Damage threshold of CuCrFeTiV high entropy alloys for nuclear fusion reactors

M. Dias [a,*], S. Magalhães [a], F. Antão [a], R.C. da Silva [a], A.P. Gonçalves [b], P.A. Carvalho [c,d], J.B. Correia [e], A. Galatanu [f], E. Alves [a]

[a] Instituto de Plasmas e Fusão Nuclear, Instituto Superior Técnico, Universidade de Lisboa, Av. Rovisco Pais, 1049-001 Lisboa, Portugal
[b] C²TN, Instituto Superior Técnico, Universidade de Lisboa, Estrada Nacional 10, 2695-066 Bobadela LRS, Portugal
[c] CeFEMA, Instituto Superior Técnico, Universidade de Lisboa, Av. Rovisco Pais, 1049-001 Lisboa, Portugal
[d] SINTEF Materials Physics, Forskningsveien 1, 0314 Oslo, Norway
[e] LNEG, Laboratório Nacional de Energia e Geologia, Estrada do Paço do Lumiar, 1649-038 Lisboa, Portugal
[f] National Institute of Materials Physics, Magurele 077125, Romania

ARTICLE INFO

ABSTRACT

A CuCrFeTiV high entropy alloy was prepared and irradiated with swift heavy ions in order to check its adequacy for use as a thermal barrier in future nuclear fusion reactors. The alloy was prepared from the elemental powders by ball milling, followed by consolidation by spark plasma sintering at 1178 K and 65 MPa. The samples were then irradiated at room temperature with 300 keV Ar^+ ions with fluences in the 3×10^{15} to 3×10^{18} Ar^+/cm^2 range to mimic neutron-induced damage accumulation during a duty cycle of a fusion reactor. Structural changes were investigated by X-ray diffraction, and scanning electron microscopy and scanning transmission electron microscopy, both coupled with X-ray energy dispersive spectroscopy. Surface irradiation damage was detected for high fluences (3×10^{18} Ar^+/cm^2) with formation of blisters of up to 1 μm in diameter. Cross-sectional scanning transmission electron microscopy showed the presence of intergranular cavities only in the sample irradiated with 3×10^{18} Ar^+/cm^2, while all irradiation experiments produced intragranular nanometric-sized bubbles with increased density for higher Ar^+ fluence. The Williamson-Hall method revealed a decrease in the average crystallite size and an increase in residual strain with increasing fluence, consistent with the formation of Ar^+ bubbles at the irradiated surface.

1. Introduction

Nuclear fusion reactors require structural and functional components able to withstand high temperatures and extreme radiation conditions. Operation at high temperatures enhances thermal efficiency and exploits advantageously the mechanical performance of the plasma facing tungsten tiles, which exhibit low toughness at moderate temperatures [1]. In this context, adequate thermal management is mandatory and requires heat extraction systems relying on materials with superior strength, creep resistance and thermal stability. In particular, microstructural stability is of paramount importance in that it guarantees that structural and thermal performances do not degrade. The presence of any strain, either built-in or developed *in loco*, can promote undesirable consequenses under operation conditions, and must thus be investigated. CuCrZr has been selected as the heat sink material for heat transfer from the plasma facing components in the first wall [2]. Unfortunaty, the service temperature of this material is relatively low (453 K < T < 623 K) [3] and it suffers embrittlement under irradiation [4]. Thus, a compatible thermal barrier interlayer between the plasma facing tungsten and the CuCrZr heat sink is required to guarantee a smooth thermal flow, which in addition may mitigate neutron induced radiation damage. A promising composite material for interlayers is the tungsten-monofilament reinforced copper composite (W_f-Cu) as suggested by Schöbel et al. [5]. However, the mismatch stress between the matrix and the filament leads to fatigue damage during thermal cycling. Another candidate class for the role are functionally graded materials (FGMs). Several authors have proposed tungsten-copper composites as FGM interlayer [4,6] but, still, a critical drawback is their loss of strength at elevated temperatures due to softening of the copper matrix [7].
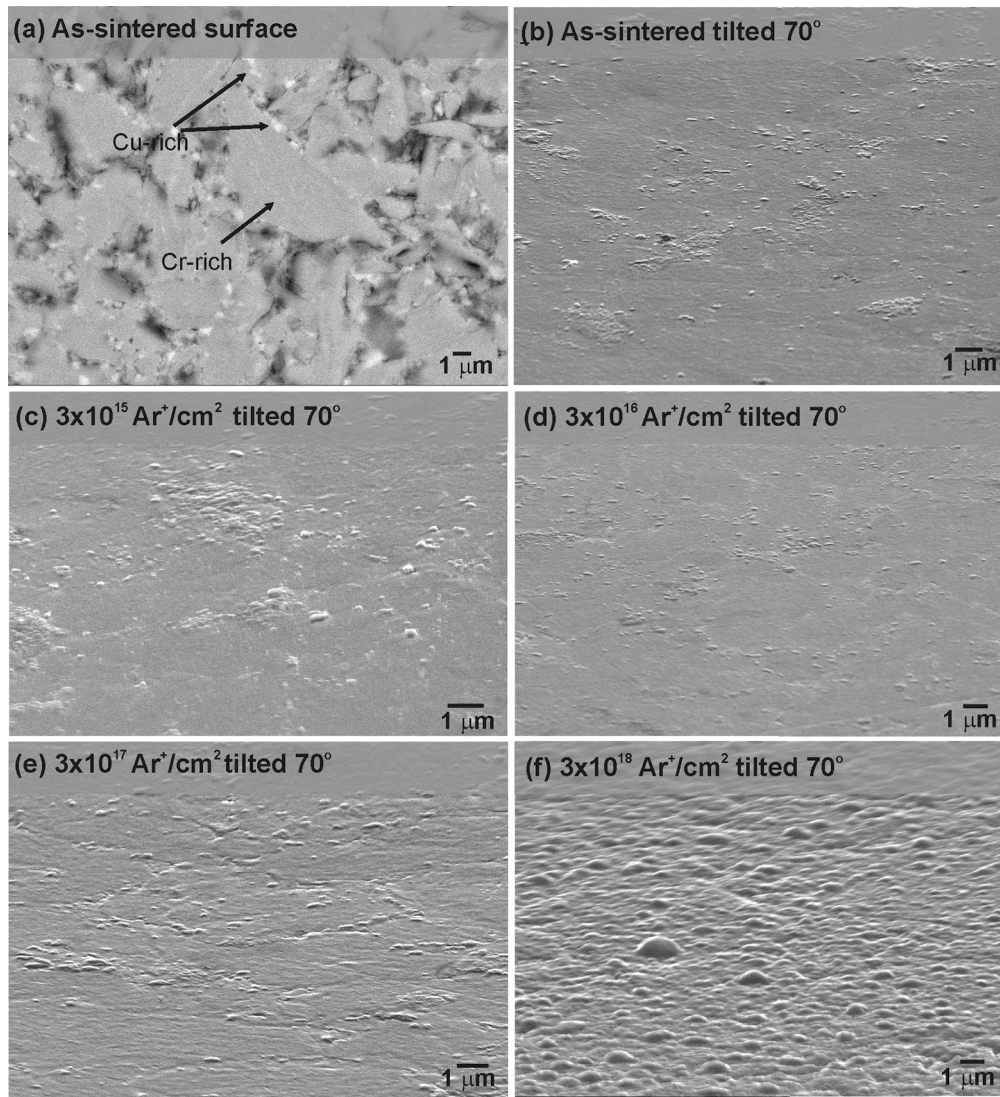

Fig. 1. Microstruture of the samples (a) and (b) as-sintered, irradiated with Ar$^+$ at fluences of (c) 3×10^{15}, (d) 3×10^{16}, (e) 3×10^{17} and (f) 3×10^{18} Ar$^+$/cm^2. (a) is a BSE image, while the remaining are SE images.

For these reasons, the use of high entropy alloys (HEAs) has been considered as a new path towards developing advanced interlayer materials. These materials possess unique properties, such as high strength and wear, oxidation and corrosion resistance, in addition to high thermal stability and intrinsically low thermal conductivity [8–12]. The ability to accumulate lattice strain confers radiation resistance to HEAs [13], but their response to damage by high energy neutrons emitted in fusion reactions is not known and requires elucidation.

In the present study, the irradiation resistance of equiatomic CuCrFeTiV is studied. The alloy was prepared by mechanical alloying (MA), followed by consolidation with spark plasma sintering (SPS) at 1178 K and 65 MPa (for details on material production see [14]). Sintered CuCrFeTiV samples were irradiated at room temperature with 300 keV Ar$^+$ beams and fluence between 3×10^{15} and 3×10^{18} ions/cm^2. The use of heavy ion irradiation as a surrogate for studying the effects of neutron damage is a standard option, justified by studies of radiation-induced defect structures in ferritic/martensitic steels arising from heavy ions vs neutrons [15,16]. In spite of expected diferences in the damage nature and distribution produced by charged ions and neutrons, this type of analysis can provide an indication of the radiation resistance potential of the alloys and their suitability as thermal barriers for fusion reactors.

Scanning electron microscopy (SEM) and scanning transmission electron microscopy (STEM), both coupled with energy dispersive X-ray spectroscopy (EDS), as well as X-ray diffraction (XRD), were used to characterize the materials. Crystallite size and strain of the as-sintered and irradiated samples are analysed and discussed.

2. Experimental

Powders of Cr, Cu, Fe, Ti and V with nominal purity higher than 99.5 % and 45 μm particle size (Alpha Aesar) were mixed in a glove box, under argon atmosphere to prevent oxidation of the metals. The powders were mechanically alloyed in a planetary ball mill (Rescht PM 400) with stainless steel vials and balls. The balls to powder mass ratio was 10:1, and milling occurred for an effective time of 20 h, at 380 rpm. Ethanol, anhydrous, was used as processing agent, to prevent heating and powder sticking to the balls and vial. The as-milled powders were next consolidated by spark-plasma sintering (SPS) in an FCT Systeme Gmbh sintering machine, at a temperature of 1178 K with a holding time of 5 min and a pressure of 65 MPa.

SRIM 2013 Monte Carlo simulations (James Ziegler - SRIM & TRIM" n.d.) were used to compute that a fluence of 3×10^{16} ions/cm^2 is needed for 300 keV Ar$^+$ ions to cause a number of defects amounting to ~ 100 dpa prior to stopping [18]. This is the average damage level expected
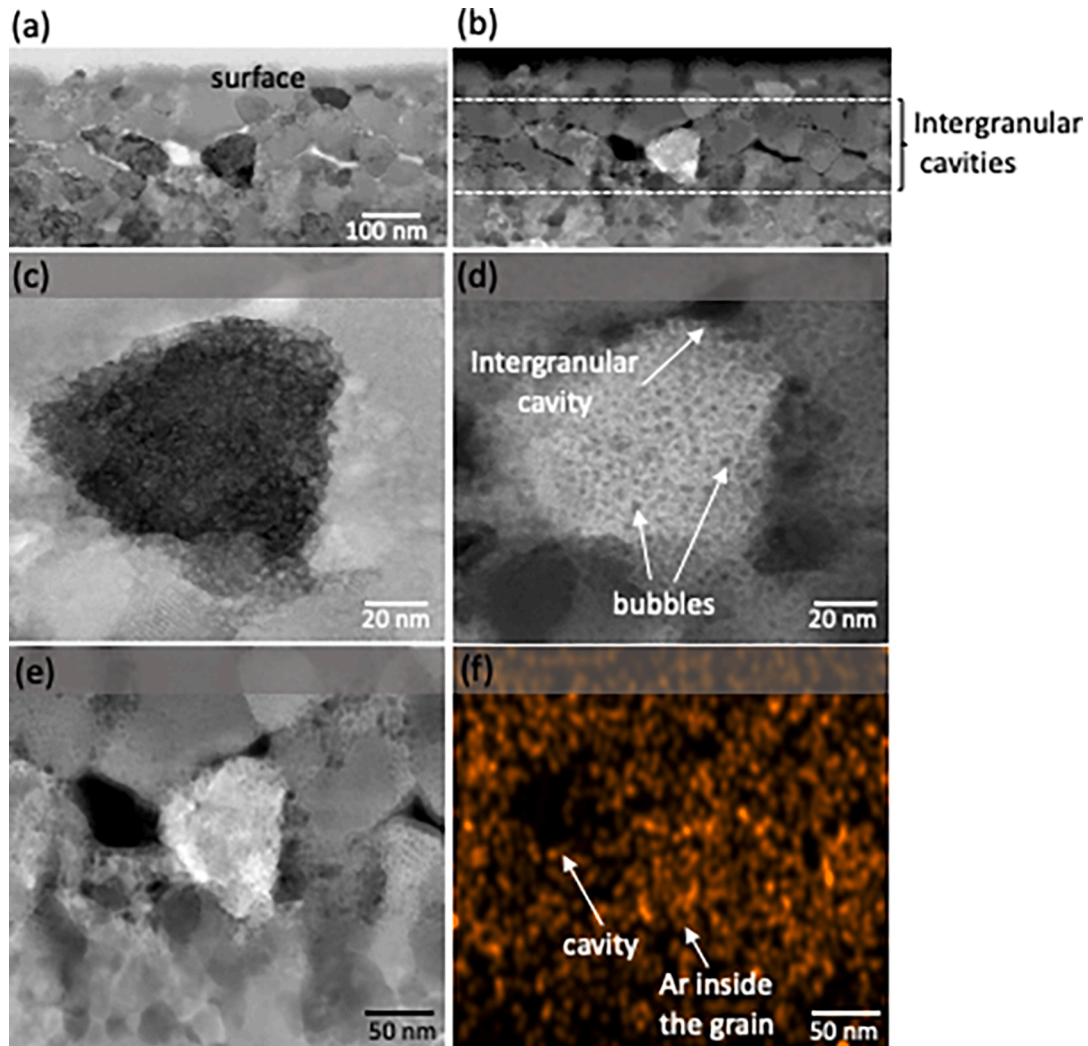
Fig. 2. (a) ABF and (b) HAADF images in cross section of the CuCrFeTiV sample irradiated with 3×10^{18} Ar$^+$/cm^2 and the corresponding magnifications (c) and (d). The image (f) is the Ar X-ray map of (e).

from neutron irradiation during the foreseeable work cycle of a fusion reactor [19]. Several samples of the sintered CuCrFeTiV high entropy alloy were irradiated at room temperature with Ar$^+$ fluences of 3×10^{15}, 3×10^{16}, 3×10^{17} or 3×10^{18} ions/cm^2. The region affected by irradiation is expected to be limited to a depth of ~ 300 nm from the surface.

Metallographic preparation of the samples was performed by grinding with SiC paper, polishing with diamond suspensions of 6 μm, 3 μm and 1 μm nominal grain size, and final fine polishing with colloidal silica suspension of 0.2 μm granulometry. The microstructures were observed before and after irradiation by secondary electrons (SE) and backscattered electrons (BSE) imaging using a JEOL JSM-7001F field emission gun SEM. The irradiated samples were observed under a tilt of 70° to better detect surface topography. The samples were also investigated by annular bright-field (ABF), low-angle annular dark field (ADF) and high-angle annular dark field (HAADF) scanning transmission electron microscopy (STEM). The transmission electron microscopy (TEM) work was performed with a DCOR Cs probe-corrected FEI Titan G2 60–300 instrument with 0.08 nm of nominal spatial resolution. Chemical information was obtained by X-ray energy dispersive spectroscopy (EDS) with a Bruker SuperX EDS system, comprising four silicon drift detectors. STEM samples were prepared using a Ga$^+$ focused ion beam with a Thermofisher Helios G4 dual beam instrument.

Due to the limited depth of the irradiated region, the X-ray diffraction was carried out in near grazing incident geometry (GIXRD), with an incident angle of 3°, using a Bruker D8 AXS diffractometer equipped with a Göebel mirror to decrease horizontal beam divergence. In these conditions, the effective penetration depth of X-rays is around 400 nm, considering the nominal density of the material (6.89 g/cm^3). A monochromator was not used to avoid the strong reduction of the diffracted intensity, instead, a Soller slit was placed in front of the scintillation detector to decrease the horizontal beam divergence.

Earlier work has shown that equimolar CuCrFeTiV HEAs prepared by SPS are microcrystalline with well defined phases [14]. Ion irradiation is expected to introduce defects that may give rise to the development of crystalline strain, leading to line broadening of the XRD patterns. In order to assess the crystallite size and strain, and correlate these with the level of radiation damage, the Williamson-Hall method was employed to analyse the XRD data. In the conditions of the Williamson-Hall model [20–24] the following condition holds:

$$B \cos\theta = \frac{K\lambda}{D} + 4\varepsilon \sin\theta \tag{1}$$

where K is the Scherrer constant, λ is the wavelength of the radiation (we used $K = 0.9$ and $\lambda = 0.154060$ nm in this work); B is the full with at half maximum (FWHM), θ represents the incident angle (half of the scattering angle), D and ε are the crystallite size and residual strain, respectively. If by plotting $B/(\lambda\cos\theta)$ vs $\sin\theta/\lambda$, a nearly straight line is found, then the apparent crystallite size and strain can be derived separately by extracting the intercept K/D and slope 4ε from the plot.
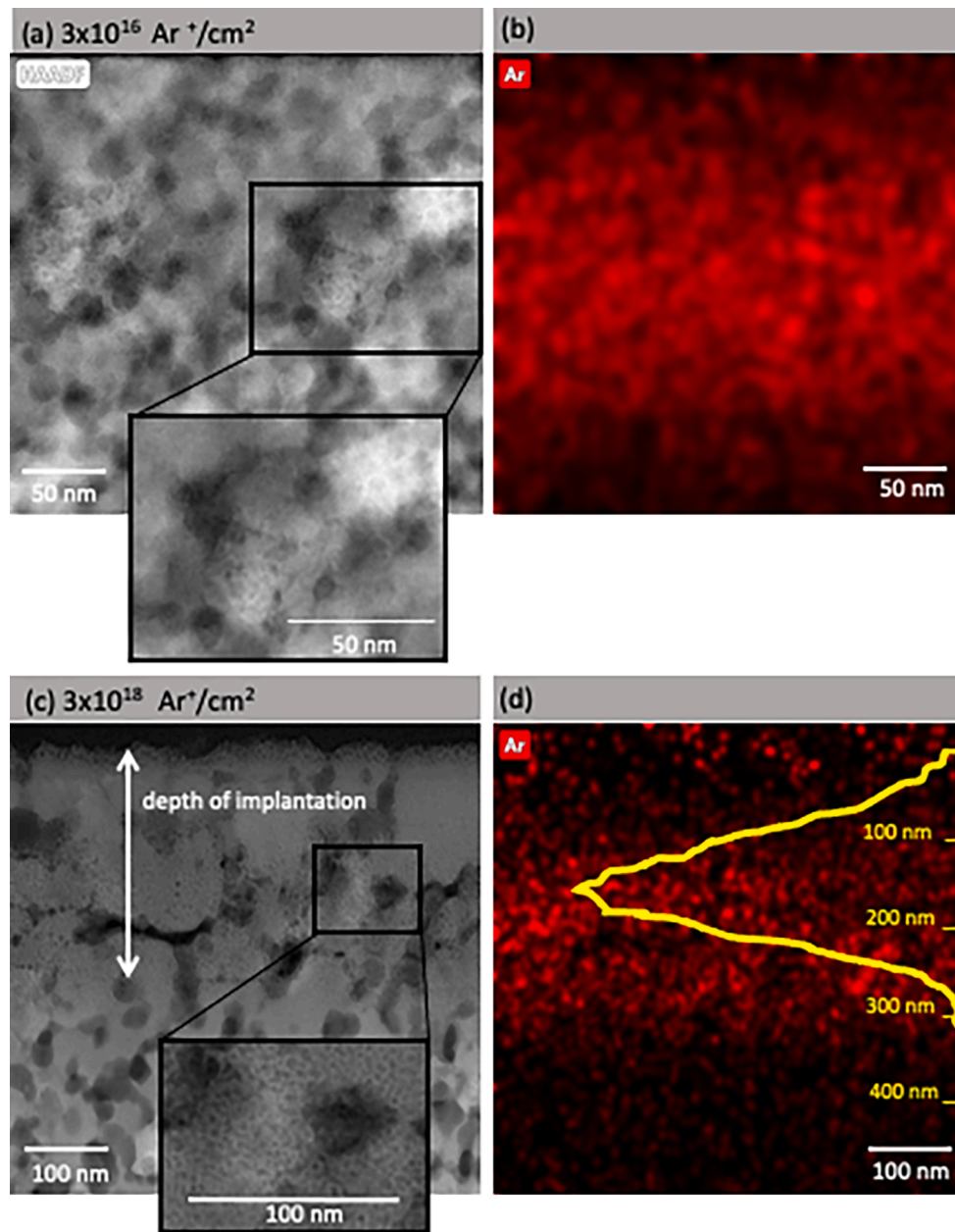
Fig. 3. (a) and (c) STEM image in cross section of the CuCrFeTiV sample irradiated with 3×10^{16} and 3×10^{18} Ar^+/cm^2 and the corresponding (b) and (d) Ar EDS maps and SRIM simulations in (d).

3. Results and discussion

The microstructure of the as-sintered CuCrFeTiV alloy is shown in Fig. 1. The sample presents two major phases, one rich in chromium while the another is rich in copper (Fig. 1 (a)) [14].

Fig. 1 (c) to (f) show the surface topography of the samples irradiated with Ar^+ with fluences between 3×10^{15} and 3×10^{18} ions/cm² at room temperature. For comparison, Fig. 1 (b) shows the surface prior to irradiation. Surface damage is visible only in the case of the highest fluence (3×10^{18} ions/cm²), with blisters of diameter predominantly<1 µm being the most evident feature (Fig. 1 (f)). It is important to point out that this fluence damage is well above, approximately 100 fold, the 100 dpa level expected from neutron irradiation after a full work cycle of a fusion reactor [19]. Therefore, as no changes were detected up to fluences of 3×10^{17} cm^{-2} (capable of inducing 10 fold more damage than expected from neutron irradiation during one duty cycle of the reactor [19], the present HEA shows high irradiation resistance.

Fig. 2 presents cross sectional STEM images of a region irradiated with 3×10^{18} Ar^+/cm^2 together with the corresponding Ar X-ray map (f). The images reveal intergranular cavities in a layer at ∼ 300 nm below the surface (bright regions in Fig. 2 (a) and dark regions in Fig. 2 (b)), while nanometric bubbles with low mass contrast are present inside the grains in this layer (see Fig. 2 (d)). As expected, the X-ray maps show that large intergranular cavities running across the thickness of the TEM lamella have been devoided of Ar during the sample preparation process, while the rare gas remained trapped in the lattice and intragranular nanometric bubbles (Fig. 2 (e) and (f)).

Fig. 3 (a) and (c) presents dark-field STEM images of samples irradiated with 3×10^{16} and 3×10^{18} Ar^+/cm^2 respectively, with the corresponding X-rays map of Ar shown in (b) and (d), on which a SRIM simulation profile for Ar is superimposed. Since the fluence of 3×10^{16} ions/cm² corresponds to the average damage level expected from neutron irradiation (100 dpa), this sample was chosen as reference to be analysed by STEM together with the sample at highest fluence, where
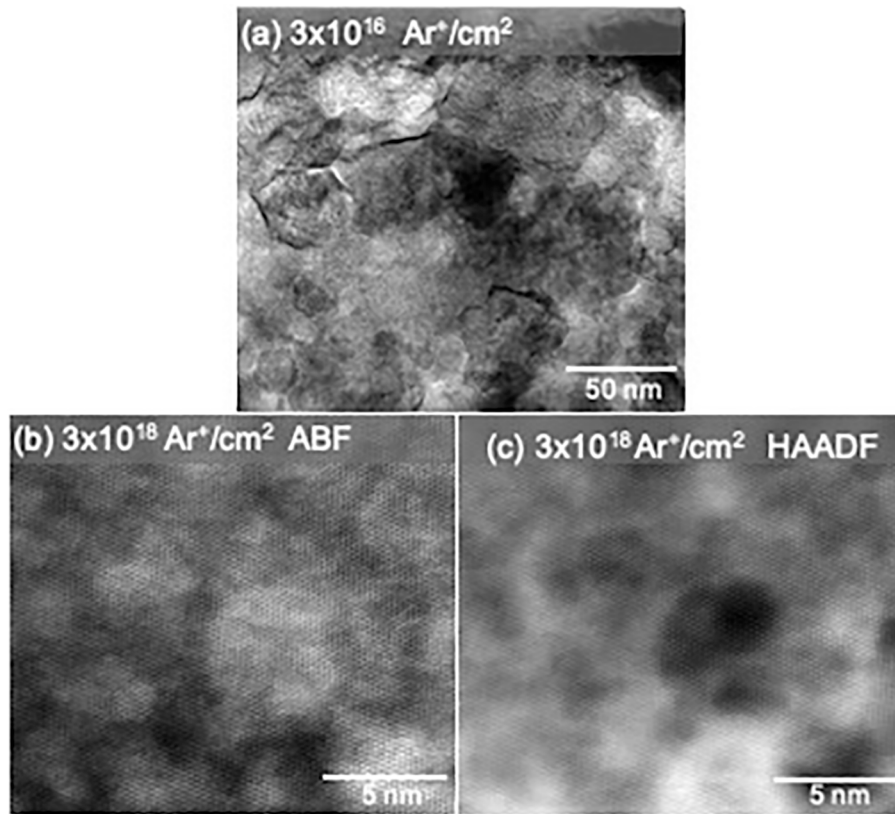
Fig. 4. STEM images in cross section of the CuCrFeTiV for the sample irradiated with (a) 3×10^{16} and (b) and (c) 3×10^{18} Ar$^+$/cm^2.

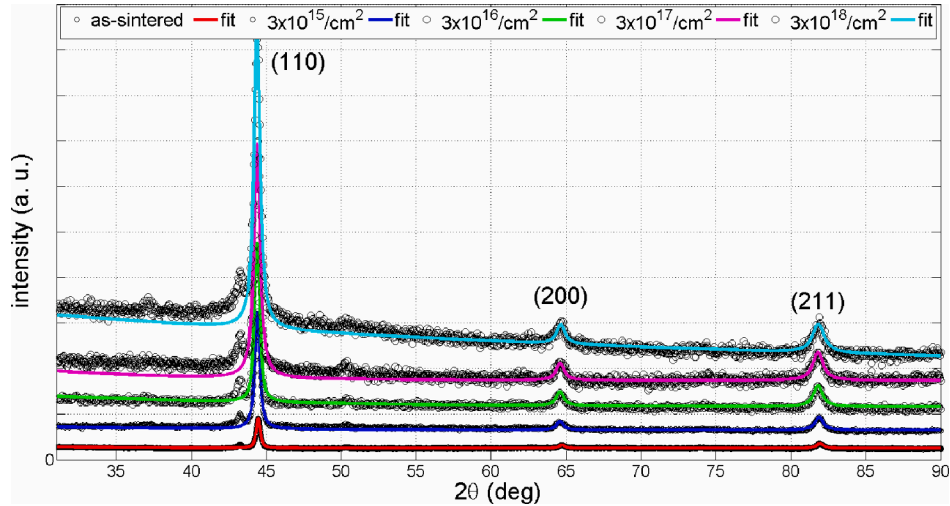**Fig. 5.** XRD diffractograms of as-sintered and irradiated samples with the Ar$^+$ fluences of 3×10^{15} Ar$^+$/cm^2, 3×10^{16} Ar$^+$/cm^2, 3×10^{17} Ar$^+$/cm^2 and 3×10^{18} Ar$^+$/cm^2. The diffractograms are vertically translated for clarity. Peaks indexed to the dominant phase, i. e. (110), (200) and (211) were fitted using a Marquardt-Levenberg algorithm. Sets of Pseudo-Voigt functions were found to best fit the peaks.

surface damage was observed by SEM. Comparing Fig. 3 (a) with 3 (c) it is possible to conclude that no intergranular cavities are present for 3×10^{16} Ar$^+$/cm^2, while the apparent intragranular bubbles density is higher for the sample irradiated with the highest fluence. It is important to point out that images presented in Fig. 3 (a) and (c) do not have the same magnification, which indicates that the bubbles generated by 3×10^{16} Ar$^+$/cm^2 are smaller than those induced by 3×10^{18} Ar$^+$/cm^2. The Ar distribution that extends to a depth of ~ 300 nm follows closely the SRIM simulations (Fig. 3 (d)). The formation of Ar$^+$ bubbles was previously studied in bcc Fe [25]. These results indicated that Ar atoms tend

to lie in substitutional sites when they cannot easily difuse through the crystal. However, in conditions of vacancy-driven mechanisms (such as in irradiation) local diffusion is enhanced and Ar forms bubbles. Moreover, if pre-existing defects such as grain boundaries or previously nucleated bubbles are present, they can be enlarged by irradiation through capture of vacancies. Therefore, a similar mechanism is expected to have been responsible for the formation of intergranular and intragranular bubbles in the present alloy.

Publications on HEAs have shown that these materials possess high irradiation resistance [13]. The self-healing capability due to the severe
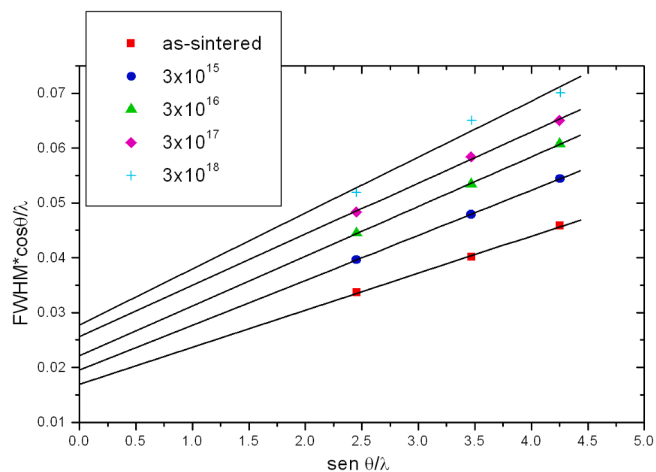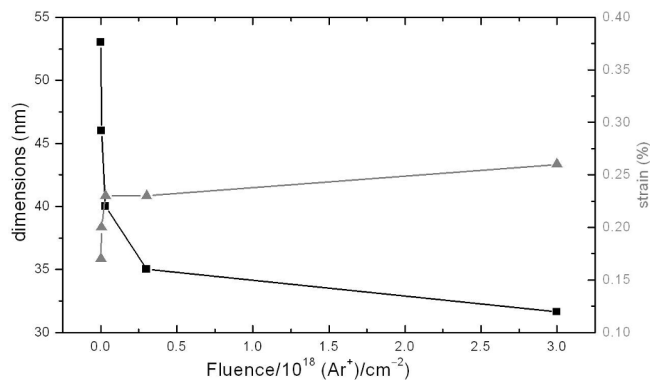
Fig. 6. Representation of $\frac{FWHM \times cos(\theta)}{\lambda}$ as function of the scattering vector norm, $\frac{sin(\theta)}{\lambda}$ for the three sets of planes (1 1 0), (2 0 0) and (2 1 1). The solid lines represent the linear fit.

Table 1
Average apparent cyrstallite sizes and strains for all samples obtained by the Williamson-Hall method.

Sample	D (nm)	ε(%)
As-sintered	53	0.17
3×10^{15}	46	0.20
3×10^{16}	40	0.23
3×10^{17}	35	0.23
3×10^{18}	34	0.26

Fig. 7. Evolution of the crystallite dimensions, and strain as function of the increasing irradiation fluences of 3×10^{15}, 3×10^{16}, 3×10^{17} and 3×10^{18} Ar^+/cm^2.

lattice distortions or atomic-level stress [26] caused by the mismatch in atom size between the principal elements was proposed as a reason for this behaviour [27].

The mottled diffraction contrast observed in the ABF STEM images shown in Fig. 4 (a) and (b) indicates that irradiation with 3×10^{16} and 3×10^{18} Ar^+/cm^2 induced the decomposition of the microcrystalline grains into crystallite mosaics with sizes 5 nm > d > 25 nm, respectively. On the other hand, the HAADF image presented in Fig. 4 (c) shows spherical intragranular bubbles with low mass contrast and characteristic dimensions < 5 nm.

Fig. 5 shows X-ray diffractograms of the as-sintered and irradiated samples. Peak indexation indicates the existence of two cubic crystal structures: a dominant body centered (bcc) phase and a minority face centered (fcc) phase (cf. [14]). A lattice parameter of 0.2879(1) nm was

assigned to the dominant bcc phase.

Fig. 6 evidences the application of the Williamson-Hall (W-H) method to the XRD reflexions (1 1 0), (2 0 0) and (2 1 1) of the dominant bcc phase indexed in Fig. 5 together with its linear fit for each fluence. Table 1 lists the average crystallite size and strain for all the samples inferred from the W-H method.

Fig. 7 shows the crystallite size and strain estimated with the W-H method as a function of irradiation fluence. In agreement with the STEM observations, these results show that the average crystallite size decreases, while strain increases with the increasing irradiation fluence. The decrease in crystallite size is quite drastic at lower fluences but seems to reach saturation at higher fluences. Irradiation tends to promote the formation of intergranular and intragranular Ar^+ bubbles observed by STEM (Fig. 2 (b) and (d)) and consequently a decrease in the crystallite size. On the other hand, strain increased with irradiation fluence which can be associated with localized lattice expansion due to the incorporation of Ar^+ ions in the material. The SRIM simulations [17] suggested a distribution of vacancies which extends through the irradiated region partially overlapping the concentration profile of the implanted Ar^+. These vacancies could agglomerate and trap Ar^+, working as nucleation sites for the formation and growth of gas pockets and bubbles. Therefore, development of high strains would be expected close to the center of the irradiated layer (see Fig. 3 (d)).

The STEM observations of irradiated samples showed that the crystallite sizes (<25 nm for the sample irradiated with 3×10^{16} Ar^+/cm^2 and < 5 nm for the sample irradiated with 3×10^{18} Ar^+/cm^2), while the W-H method indicates for the same samples a different values (40 and 34 nm, respectively (Table 1)). In general, the apparent crystallite sizes derived via the W-H method are expected to be in average closer than those observed by TEM. However, in the present case, the difference between these values can be attributed to the fact that X-ray analysis averages penetration depth is about 400 nm, while the particle size calculated from STEM images corresponds to the average radius of the crystalline domains observed only at a layer with a thickness of about 100 nm. In other words, a crystallite size limited to 400 nm corresponds to the X-rays effective penetration depth quantified as ~ 33 % higher than the implanted argon region (300 nm given by SRIM calculations, Fig. 3 (d)). In fact, in the case of the former, the W-H method determines the averaged crystallite size within the probed 400 nm of effective penetration depth and not the crystallite size as a result of scattering events arising uniquely from the implanted region - the extra 100 nm probed will contribute to an increase in the W-H derived averaged crystallite size. Moreover, the W-H analysis is performed from the combination of the (1 1 0), (2 0 0) and (2 1 1) Bragg peaks indexed to the CuCrFeTiV high entropy alloy and no extra Bragg peaks are observed after implantation. Therefore, the W-H analysis is put forward to the probed CuCrFeTiV volume and is not restricted to the implantation region. Another reason for these diference between the two tecniques is the fact that the material is heterogeneous, which can hinder some effects (few TEM lamellas can be observed) while W-H method is applied generaly to homogenous materials.

To sum up, since no blistering at the surface was detected and only low bubble density was observed in the cross-sections after irradiation with 3×10^{16} Ar^+/cm^2 (100 dpa), the present results indicate that the CuCrFeTiV high entropy alloy presents high radiation resistance and can be regarded as a potential candidate for thermal barriers.

4. Conclusions

CuCrFeTiV high entropy alloys were prepared by mechanical alloying and spark plasma sintering and studied by scanning and transmission electron microscopy and X-ray diffraction. The samples were subsequently irradiated at room temperature with 300 keV Ar^+ ions with fluences in the range of 3×10^{15} to 3×10^{18} ions/cm^2. The microstructural results showed that surface blistering occured for irradiation with 3×10^{18} to Ar^+/cm^2. Cross-sectional scanning transmission

electron microscopy images revealed the presence intergranular cavities in the sample irradiated with 3×10^{18} Ar$^+$/cm^2. The materials irradiated presented intragranular nanometric bubbles, albeit the apparent density of these defects was much lower after irradiation with 3×10^{16} Ar$^+$/cm^2 than 3×10^{18} Ar$^+$/cm^2. X-ray diffraction analysis showed a decrease of the apparent crystallite size with increasing fluence due to formation of bubbles in the Ar$^+$ irradiated layer. Strain increased initially with the irradiation fluence which can be associated with extreme levels of deformation owing to incorporation of Ar$^+$ ions in the material. In view of the findings presented in this work, whereby no significant structural or morphologic alterations were detected for irradiation fluences up to 3×10^{17} Ar$^+$/cm^{-2}, which corresponds to 10 × the targeted design fluence, we anticipate that CuCrFeTiV alloy full-fills is a potential candidate for thermal barrier material in future nuclear fusion reactors.

Declaration of Competing Interest

The authors declare that they have no known competing financial interests or personal relationships that could have appeared to influence the work reported in this paper.

Data availability

Data will be made available on request.

Acknowledgements

References

[1] ASM International. Handbook Committee., *ASM handbook*.
[2] V. Barabash *et al.*, "Materials challenges for ITER - Current status and future activities," *J. Nucl. Mater.*, vol. 367-370 A, no. SPEC. ISS., pp. 21–32, 2007.
[3] D. Stork, et al., Developing structural, high-heat flux and plasma facing materials for a near-term DEMO fusion power plant: The EU assessment, J. Nucl. Mater. 455 (1–3) (2014) 277–291.
[4] T.R. Barrett, et al., Enhancing the DEMO divertor target by interlayer engineering, Fusion Eng. Design 98–99 (2015) 1216–1220.
[5] M. Schöbel, et al., Thermal cycling stresses in W-monofilament reinforced copper, Adv. Eng. Mater. 13 (8) (2011) 742–746.
[6] Z.J. Zhou, S.X. Song, J. Du, Z.H. Zhong, C.C. Ge, Performance of W/Cu FGM based plasma facing components under high heat load test, J. Nucl. Mater. 363–365 (1–3) (2007) 1309–1314.
[7] J.-H. You, A. Brendel, S. Nawka, T. Schubert, B. Kieback, Thermal and mechanical properties of infiltrated W/CuCrZr composite materials for functionally graded heat sink application, J. Nucl. Mater. 438 (1–3) (2013) 1–6.
[8] C.-Y. Hsu, J.-W. Yeh, S.-K. Chen, T.-T. Shun, Wear resistance and high-temperature compression strength of Fcc CuCoNiCrAl0.5Fe alloy with boron addition, Metall. Mater. Trans. A 35 (5) (2004) 1465–1469.
[9] P.-K. Huang, J.-W. Yeh, T.-T. Shun, S.-K. Chen, Multi-Principal-Element Alloys with Improved Oxidation and Wear Resistance for Thermal Spray Coating, Adv. Eng. Mater. 6 (12) (2004) 74–78.
[10] Y.Y. Chen, U.T. Hong, H.C. Shih, J.W. Yeh, T. Duval, Electrochemical kinetics of the high entropy alloys in aqueous environments - A comparison with type 304 stainless steel, Corros. Sci. 47 (11) (2005) 2679–2699.
[11] M.-H. Tsai, et al., Thermal Stability and Performance of NbSiTaTiZr High-Entropy Alloy Barrier for Copper Metallization, J. Electrochem. Soc. 158 (11) (2011) H1161.
[12] C.-L. Lu, S.-Y. Lu, J.-W. Yeh, W.-K. Hsu, Thermal expansion and enhanced heat transfer in high-entropy alloys, J. Appl. Cryst 46 (2013) 736–739.
[13] T. Egami, W. Guo, P.D. Rack, T. Nagase, Irradiation resistance of multicomponent alloys, Metall. Mater. Trans. A Phys. Metall. Mater. Sci. 45 (1) (2014) 180–183.
[14] M. Dias, et al., Sintering and irradiation of copper-based high entropy alloys for nuclear fusion, Fusion Eng. Design 146 (2019) 1824–1828.
[15] G.L. Kulcinski, A.B. Wittkower, G. Ryding, Use of heavy ions from a tandem accelerator to simulate high fluence, fast neutron damage in metals, Nucl. Instruments Methods 94 (2) (1971) 365–375.
[16] G.S. Was, Challenges to the use of ion irradiation for emulating reactor irradiation, J. Mater. Res. 30 (9) (2015) 1158–1182.
[17] "James Ziegler - SRIM & TRIM." [Online]. Available: http://www.srim.org/. [Accessed: 30-Mar-2020].
[18] N. Baluc, et al., Status of R&D activities on materials for fusion power reactors, Nucl. Fusion 47 (10) (2007) S696–S717.
[19] M. R. Gilbert, S. L. Dudarev, D. Nguyen-Manh, S. Zheng, L. W. Packer, and J.-C. Sublet, "Neutron-induced dpa, transmutations, gas production, and helium embrittlement of fusion materials," Nov. 2013.
[20] B.E. Warren, B.L. Averbach, The effect of cold-work distortion on x-ray patterns, J. Appl. Phys. 21 (6) (1950) 595–599.
[21] M. Rafiei, M.H. Enayati, F. Karimzadeh, Characterization and formation mechanism of nanocrystalline (Fe, Ti)3Al intermetallic compound prepared by mechanical alloying, J. Alloys Compd. 480 (2) (2009) 392–396.
[22] A. Khajesarvi, G.H. Akbari, Synthesis and Characterization of Nanocrystalline Ni 50 Al 50−x Mo x (x = 0–5) Intermetallic Compound during Mechanical Alloying Process, J. Nanoparticles 2015 (2015) 1–6.
[23] A. Heczel, M. Kawasaki, J.L. Lábár, J. Il Jang, T.G. Langdon, J. Gubicza, Defect structure and hardness in nanocrystalline CoCrFeMnNi High-Entropy Alloy processed by High-Pressure Torsion, J. Alloys Compd. 711 (2017) 143–154.
[24] S. Vives, E. Gaffet, C. Meunier, X-ray diffraction line profile analysis of iron ball milled powders, Mater. Sci. Eng. A 366 (2) (2004) 229–238.
[25] X. Gai, R. Smith, S.D. Kenny, Inert gas bubbles in bcc Fe, J. Nucl. Mater. 470 (2016) 84–89.
[26] T. Nagase, P.D. Rack, J.H. Noh, T. Egami, In-situ TEM observation of structural changes in nano-crystalline CoCrCuFeNi multicomponent high-entropy alloy (HEA) under fast electron irradiation by high voltage electron microscopy (HVEM), Intermetallics 59 (2015) 32–42.
[27] I. Toda-Caraballo, P.E.J. Rivera-Díaz-Del-Castillo, Modelling solid solution hardening in high entropy alloys, Acta Mater. 85 (2015) 14–23.